PNAS
www.pnas.org

Supplementary Information for

Robust nanoscopy of a synaptic protein in living mice by organic-fluorophore labeling

Jennifer-Magdalena Masch[a,b], Heinz Steffens[a] , Joachim Fischer[c], Johann Engelhardt[c,d], Jasmine Hubrich[a], Jan Keller-Findeisen[a], Elisa D'Este[a], Nicolai T. Urban[a,b], Seth G. N. Grant[e], Steffen J. Sahl[a], Dirk Kamin[a,b,1], and Stefan W. Hell[a,b,c,d,1]

[a]Department of NanoBiophotonics, Max Planck Institute for Biophysical Chemistry, 37077 Göttingen, Germany
[b]Center for Nanoscale Microscopy and Molecular Physiology of the Brain (CNMPB), 37073 Göttingen, Germany
[c]Optical Nanoscopy Division, German Cancer Research Center (DKFZ), 69120 Heidelberg, Germany
[d]Department of Optical Nanoscopy, Max Planck Institute for Medical Research, 69120 Heidelberg, Germany
[e]Centre for Clinical Brain Sciences, Edinburgh University, Edinburgh EH16 4SB, United Kingdom

[1]Corresponding authors: Dirk Kamin (dirk.kamin@mpibpc.mpg.de) and Stefan W. Hell (stefan.hell@ mpibpc.mpg.de)

This PDF file includes:

www.pnas.org/cgi/doi/10.1073/pnas.1807104115

SI Materials and Methods

Mouse Lines. PSD95-HaloTag male mice of age 3−6 mo, both heterozygous and homozygous, were used in this study.

The data in *SI Appendix*, Fig. S7, showing imaging capabilities with PSD95 fusions to far-red FPs, was obtained with a C57BL/6N wildtype mouse (for mNeptune2) and a transgenic Thy1.2-EYFP transgenic mouse (B6N.FVB-tg(mThy1.2-EYFP)Fki; ref. 1; kindly provided by the laboratory of F. Kirchhoff, University of Saarland, Germany) expressing yellow FPs in a subset of cortical neurons in layer V (for mGarnet). Mice were 3−6 mo old and male.

Plasmid Generation. pAAV-hSyn-Lifeact-EYFP was cloned as previously reported (2) from the pAAV-hSyn-EYFP plasmid, kindly provided by the laboratory of K. Deisseroth (Stanford University, CA, USA). The two plasmids were used as templates for the other plasmids in this work.

The plasmid for pAAV-hSyn-EGFP was engineered by PCR amplification of the coding sequence of EGFP using the forward primer 5′-CATACGGATCCGATGGTGAGCAAGGGCGAGGA-3′ (*BamH*I) and the reverse primer 3′-CCTGAATTCCAGTTACTTGTACAGCTCGTCCATG-5′ (*EcoR*I). The fragment was ligated into the equally digested backbone of the pAAV-hSyn-EYFP plasmid using *BamH*I and *EcoR*I restriction enzymes.

The pAAV-hSyn-PSD95-mNeptune2 plasmid was generated on the basis of a PSD95-EGFP plasmid, a kind gift from the laboratory of T. Bonhoeffer (Max Planck Institute of Neurobiology, Germany). PSD95 was PCR-amplified from the PSD95-EGFP plasmid using the forward primer 5′-TCGATCGGTACCGGATCCAATGGACTGTCT CTGTATA-3′ (*Kpn*I) and the reverse primer 3′-GTAGCTACCGGTGCGTCCCCGAGTCTCTCTCGGGCTGG-5′ (*Age*I) and ligated into the equally digested pAAV-hSyn-Lifeact-mNeptune2 vector which was generated on the basis of the pAAV-hSyn-Lifeact-EYFP vector with mNeptune2 in between the restriction sites of *Age*I and *EcoR*I.

The plasmid pAAV-hSyn-PSD95-mGarnet was generated by amplifiying the coding sequence of mGarnet using the forward primer 5′-TCAGAACCCGGGAATGAACAGCCTGATCAAA-3′ (*Xma*l) and the reverse primer 3′-ACTTAGGAATTCCTAGATTTTCACCCTCCG -5′ (*EcoR*I) from the CMV-Lifeact-mGarnet plasmid kindly provided by the laboratory of G. U. Nienhaus (Karlsruhe Institute of Technology, Germany; ref. 3). The digested mGarnet fragment was ligated into the backbone of the pAAV-hSyn-PSD95-mNeptune2 plasmid (mNeptune2 was removed by *Age*I (compatible cohesive end to *Xma*l) and *EcoR*I).

Viral Vector Production. To obtain recombinant adeno-associated viral (rAAV) vectors of mixed serotype 1 and 2, HEK 293FT cells were transfected with the following plasmids: the pAAV plasmid encoding the protein of interest, the pFdelta6 adenovirus helper plasmid, and pH21 and pRV1 plasmids containing replication and capsid protein sequences for serotype 1 and 2, respectively. After 2 d, the cells were resuspended in lysis buffer (NaCl 150 mM, Tris-HCl 50 mM; pH 8.5), cracked by 3 freeze-thaw cycles (-80°C for 20 min, 37°C for 10 min) and treated with 1 µl/ml DNAseI (1 unit/µl; 37°C for 30 min). The lysate was centrifuged (1,690 g for 10 min) to remove all cell fragments, and the supernatant was centrifuged in a second round to pellet the virus particles (48,000 g for 2 h at 4°C). The pellet was resuspended in 150 µl sterile PBS (pH 7.4) and aliquots were stored at -80°C.

Animal Procedures. All animal procedures were conducted in accordance with the Animal Welfare Law of the Federal Republic of Germany (Tierschutzgesetz der Bundesrepublik Deutschland, TierSchG) and the regulation about animals used in experiments (Tierschutzversuchsverordnung), and were approved and authorized by the Niedersächsisches Landesamt für Verbraucherschutz und Lebensmittelsicherheit (LAVES, Oldenburg, Germany). During all surgical procedures and in vivo STED imaging, the mouse was always kept on a heating plate to maintain its body temperature. Vital functions and the depth of anesthesia were continuously monitored using a pulse oximeter (MouseOx Plus, Starr Life Sciences Corp., Oakmont, PA, USA) and electrocardiogram (ECG) recordings with a home-built device (no ECG recording during virus transductions).

Virus Transduction. Virus transductions were performed by stereotactic intracranial injections of recombinant adeno-associated viral vectors (rAAV; mixed serotype 1 and 2) 2−4 wk prior to the in vivo STED imaging. All surgical steps were performed under sterile conditions. The mouse was preemptively analgized by subcutaneous injection of carprofen (5 mg/kg body weight; 50 mg/ml carprofen in sterile 0.9 % NaCl; Rimadyl, Pfizer, New York City, NY, USA; NaCl, B. Braun Melsungen, Melsungen, Germany). At least 30 min after analgesia administration, anesthesia was initiated by intraperitoneal injection of pentobarbital sodium (77 mg/kg body weight; 16 g/100ml pentobarbital sodium in sterile 0.9 % NaCl; Narcoren, Merial, Hallbergmoos, Germany). The mouse was placed in prone position on a heating plate (home-built) with its head mounted in a stereotactic frame (SG-4N, Narishige, Tokyo, Japan), breathing through a respiratory mask (home-built; gas mixture: 47.5 % oxygen, 50 % nitrogen, and 2.5 % carbon

dioxide; Westfalen AG, Münster, Germany). The shaved and disinfected head was surgically opened by a ~5 mm incision, and a ~0.7 mm hole was drilled through the skull of the left parietal bone above the visual cortex (stereotactic coordinates: 2.5 mm lateral to the midline, 4.0 mm posterior to bregma, ref. 4). The trepanation was perforated carefully with forceps to expose the underlying cortex and was kept moist with sterile artificial cerebrospinal fluid (ACSF; NaCl 126 mM, KCl 2.5 mM, $CaCl_2$ 2.5 mM, MgCl 1.3 mM, HEPES 27 mM, glucose 30 mM; pH 7.4). A pre-pulled glass micropipette (tip diameter ~10 µm (1B150F-4, 0.84 mm inner diameter (ID), 1.5 mm outer diameter (OD); World Precision Instruments, Sarasota, FL, USA) was inserted with a feed of ~700 µm under an angle of 20° to the horizontal axis to reach the region containing cell bodies of pyramidal neurons in layer V at a depth of ~500 µm (*SI Appendix*, Fig. S3*A*). Approximately 250−500 nl rAAV-mixture (virus diluted 1:5 in sterile ACSF) was injected using air-pressured pulses (30 to 50 msec pulses with 0.7 to 3.5 bar; parameters were adjusted to modulate the flow rate; TooheySpritzer, Toohey Company, Fairfield, NJ, USA). The scalp incision was closed with single-button sutures, the mouse was placed back in the cage to recover (supported on a heating plate), and was then returned to the animal care unit for 2−4 wk until the imaging experiment. For post-operative care, the mouse was analgized with metamizole in the drinking water for the following 3 d (375 mg/250ml; Novaminsulfon, Ratiopharm, Ulm, Germany).

Surgical Preparation for in Vivo STED Imaging. The surgical preparation for in vivo STED imaging followed the previously reported protocols (2, 5). Preemptive analgesia was initiated by subcutaneous injection of carprofen (5 mg/kg of body weight; 50 mg/ml carprofen in sterile physiological 0.9 % NaCl), followed by initial anesthesia using intraperitoneal injection of pentobarbital sodium after 30 min (77 mg/kg of body weight; 16 g/100ml pentobarbital sodium dissolved in sterile physiological 0.9 % NaCl; Narcoren, Merial; NaCl, B. Braun Melsungen). The mouse was placed in supine position on a heating plate (home-built) with a respiratory mask (home-built). The throat was exposed by a skin incision to gain access to the right external jugular vein for vascular catheterization with a fine tube catheter (Portex™ Fine-Bore Polyethylene Tubing, ID: 0.28 mm, OD: 0.61 mm, Smiths Medical, St. Paul, MN, USA). Anesthesia was then sustained by continuous infusion of methohexital sodium (50 mg/h/kg body weight; 500 mg methohexital sodium dissolved in sterile physiological 0.9 % NaCl, Brevimytal, Hikma, London, UK). A home-built, T-shaped tube was inserted into the trachea by performing a tracheotomy. The mouse was artificially ventilated (120 breaths/min, tidal volume 120−140 µl) and paralyzed by subcutaneous injection of pancuronium bromide (100 µl/hr, 0.095 mg/ml stock solution; 2 mg/ml pancuronium bromide dissolved in sterile 0.9 % NaCl; Pancuronium, Inresa, Freiburg, Germany). In preparation for a cranial window, the head of the mouse was shaved, the scalp was surgically removed, the periosteum was carefully scraped off the bone, and Histoacryl tissue adhesive (B. Braun Melsungen) was applied to the wound margins to keep the skull dry (*SI Appendix*, Fig. S3*B*). The mouse head was immobilized with a flat, tiltable, T-shaped head holder (home-built), which was adhered with dental cement (Super-Bond CB, Sun Medical Co., Moriyama City, Japan) to the frontal bone part of the skull. Access to the visual cortex was provided by drilling a circular groove (2 to 3 mm ID) into the skull, compromising the trepanation utilized for rAAV transduction. A fine tube (150 µm OD), filled with ACSF and connected to a syringe, was inserted at the edge of the groove to extract spare cerebrospinal fluid during imaging if necessary. While covered with ACSF, the circular cranial bone was lifted and extracted carefully. Residual bone material and the arachnoid mater were then removed. Except for experiments with FP labeling of PSD95 (*SI Appendix*, Fig. S7), the fluorescent ligand silicon-rhodamine HaloTag (SiR-Halo) was stereotactically injected at multiple sites near the center of the cranial window (see *SI Appendix*, *In Vivo Labeling*). Afterwards, the cranial hole was covered with a coated circular cover glass (6 mm diameter, #1.5 thickness; Thermo Fisher Scientific, Waltham, Massachusetts, USA) and sealed with Histoacryl tissue adhesive. A sparse layer of 100-nm fluorescent Crimson beads (Invitrogen, Carlsbad, California, USA) coated onto the cover glass side facing the brain served as a cross reference for the depth of the imaging plane. Finally, the exposed skull, wound margins, edges of the cover glass, and the head holder were sealed with dental cement for mechanical stability (*SI Appendix*, Fig. S3*B*). The head-fixed mouse was placed on the translation stage with a cranial window adjusted perpendicular to the optical axis of the microscope. After the imaging experiment, the mouse was perfused with paraformaldehyde for histological analysis (see *SI Appendix*, *Histology*).

In Vivo Labeling. A method for in vivo labeling of endogenous PSD95-HaloTag fusion proteins with a fluorescent organic HaloTag ligand, here SiR-Halo, was established by direct intracortical injections of SiR-Halo into the central area of the cranial window. The HaloTag-derivative of SiR was custom-made following the synthesis described in ref. 6. For in vivo labeling, a pre-pulled glass micropipette (~10 µm tip diameter, 1B150F-4, ID: 0.84 mm, OD: 1.5 mm; World Precision Instruments) was stereotactically inserted with a feed of 100 µm into the first layer of the visual cortex under an angle of 20° to the horizontal axis. A volume of 100 to 250 nl SiR-Halo (750 nM, dissolved in ACSF) was

injected using air-pressured pulses (30 to 50 msec pulses with 0.7 to 3.5 bar). The SiR-Halo injections were performed at multiple sites within the center of the cranial window in between the superficial blood vessels (Fig. 1 *A* and *C*).

Histology. The mouse was transcardially perfused with PBS (pH 7.4), followed by PFA (4 % in PBS, pH 7.4). The dissected brain was post-fixed in 4 % PFA at 4°C over-night, and serial coronal sections of 70 µm thickness were cut from the agarose-embedded (3 % in PBS) left hemisphere using a vibratome (VT 1000S, Leica). Sections placed on coverslips were mounted in Mowiol for epifluorescence imaging (DM6000 B, Leica Microsystems GmbH, Wetzlar, Germany).

In Vivo STED Nanoscope. *SI Appendix*, Fig. S1 shows the home-built STED nanoscope, designed for in vivo STED imaging in the far-red to near-IR spectrum. A major design constraint was the upright configuration of the objective lens to accommodate the mouse head's orientation in prone position. Further, optical beam path lengths were minimized throughout the setup for highest optical stability. The microscope setup was constructed in a modular fashion (an excitation module, a module with the laser source for deexcitation by STED, a STED unit, and a detection module) around an upright microscope stand (DM6000 FS, Leica Microsystems), equipped with standard filter sets, a 63× glycerol-immersion objective lens (*NA*=1.30, n=1.46; HC PL APO 63×/1.30 GLYC CORR CS2, Leica Microsystems) and an independent motorized xyz-translation stage (380FM-U, Luigs und Neumann Feinmechanik + Elektrotechnik GmbH, Ratingen, Germany) for mouse positioning.

Fluorophores with far-red to near-IR emission were excited by one of the two pulsed excitation lasers (594 nm, 200 µW, custom-built, ref. 7; 640 nm, 2 mW, LDH-D-C-640, PicoQuant, Berlin, Germany) with pulses of ≤130 ps length, externally triggered by the STED laser operating at 80 MHz repetition rate. A continuous wave (CW) laser (473 nm 100 mW, 06-MLD, Cobolt AB, Solna, Sweden) was additionally installed for exciting EYFP/EGFP fluorescence. The three excitation laser beams were coupled into a 2-m-long polarization-maintaining single-mode fiber (PMC-460-3.0-NA012-3-APC-200-P, Schäfter+Kirchhoff GmbH, Hamburg, Germany) by using a combination of a dispersive equilateral prism (PS859, Thorlabs Inc., Newton, New Jersey, USA) and an acousto-optic tunable filter (AOTF, AOTFnc-VIS-TN, AA Opto-Electronic, Orsay, France). The latter also allowed to vary the excitation laser powers.

The STED beam was provided by a Titanium-Sapphire laser (Mai Tai XF-W1S, Spectra-Physics, Inc., Santa Clara, CA, USA) emitting ~80 fs laser pulses at 775 nm with a repetition rate of ~80 MHz. The STED pulses were stretched to about 300 ps by passing the beam through two 19-cm-long, highly dispersive SF6 glass rods (home-manufactured) and a 100-m-long polarization-maintaining single-mode fiber (PM630-HP, Thorlabs). The STED laser power was modulated by an electro-optic modulator (EOM, LM 0202 P VIS, Linos AG, Göttingen, Germany). The 8 % reflection from a pellicle beam splitter (BP108, Thorlabs) placed before the EOM was used to generate a trigger signal for the excitation lasers and the time-gated detection through a custom-made unit consisting of a photodiode and a constant fraction discriminator. The beam emerging from the fiber was collimated and guided onto a liquid-crystal-based spatial light modulator (SLM, X10468-12(X), Hamamatsu Photonics K.K., Hamamatsu, Japan) applying a helical phase profile (0–2π) to the wavefront of the STED beam, which resulted in a doughnut-shaped beam profile with a central intensity zero in the focal plane after focusing by the objective lens. The applied phase pattern on the SLM comprised of the helical phase pattern, which was superposed with a blazed grating in order to separate the phase-modified beam (first diffraction order) from unmodulated beam components (zeroth diffraction order). A wedge prism (PS812-B, Thorlabs) after the SLM compensated the spectral dispersion induced by the blazed grating. The STED beam passed a pinhole which removed the zeroth diffraction order and then traversed a bandpass filter (BP1, ET780/40m, Chroma Technology Corp., Bellows Falls, VT, USA) to reduce the spectral broadening due to self-phase modulation.

The STED beam was then co-axially combined with the excitation beams via a dichroic mirror (DM1, T680 LPXXR, Chroma). The circular polarization of the co-aligned beams was adjusted with an achromatic half-wave plate and an achromatic quarter-wave plate (both: Bernhard Halle Nachfolger GmbH, Berlin, Germany). The beams entered the microscope stand through an achromatic scan lens (f=100 mm VIS, G052015000, Qioptiq Photonics GmbH & Co. KG, Göttingen, Germany) and a home-built beam scanner (Quadscanner, ref. 8, 9), which consisted of four galvanometric mirrors scanning the beams in both lateral directions with a maximum field of view (FOV) of 130 µm × 130 µm. A tube lens (Leica Microsystems) relayed the intermediate image plane within the beam scanner to the pupil of the high-*NA* 63× glycerol-immersion objective lens, mounted on a piezoelectric microscope lens positioner (zPiezo, MIPOS 100 PL CAP M25, piezosystem jena GmbH, Jena, Germany) for fine z-positioning. The objective lens focused all the beams onto the sample.

The fluorescence emission was collected by the same objective lens, descanned by passing back through the beam scanner, and finally separated from the STED and the excitation laser beams using a custom-made dichroic mirror

(DM2, ZT473/594/640/745-800tpc-UF3, Chroma). The out-of-focus light was reduced by a motorized pinhole (Variable Pinhole TCS 2, Leica Microsystems) with a typical diameter of 50 µm, whose backprojected size corresponded to 1.2 Airy units of the fluorescence wavelength of 685 nm. The fluorescence was then filtered by a shortpass filter (SP1, ET720 SP-2P, Chroma) and coupled into a 2-m-long multi-mode fiber (MMF, FG050LGA-Custom-Muc, Thorlabs). The fiber emission was split into three detection channels using two optical filters (LP20°, longpass filter at 20° angle of incidence, BLP01-594R-25, Semrock, Inc., Rochester, NY, USA; SP13°, shortpass filter at 13° angle of incidence, FF01-655/SP-25, Semrock). In each detection channel, the fluorescence signal was spectrally filtered (green-yellow: BP2, FF03-525/50-25, Semrock; red: BP3, FF01-623/24-25, Semrock; dark-red: BP4, ET685/70m, Chroma) and focused onto a free-space avalanche photodiode module (APD, SPCM-ACRH-13, Excelitas Technologies Corp., Waltham, MA, USA). The fluorescence photons were counted by the APDs and relayed to a field-programmable gate array (FPGA, PCIe-7852R, National Instruments Corp., Austin, TX, USA), which was also used for hardware control of the STED nanoscope. The timings of excitation, detection and scanning were synchronized to the pulses of the STED laser. For best STED performance, the excitation laser pulse was adjusted ~150 ps before the STED laser pulse (peak-to-peak), and fluorescence was detected starting ~0.35 ns after the STED laser pulse for a duration of 9 ns (gate width).

Image Acquisition. The STED nanoscope and its image acquisition were controlled by a graphical user interface based on a custom-written code in LabVIEW (National Instruments), with the exception of the SLM, which was controlled by an interface programmed in MATLAB (The MathWorks, Inc., Natick, MA, USA). We performed in vivo imaging at a depth of 5−25 µm below the cortical surface and adjusted the imaging parameters (*SI Appendix*, Table S1) and the correction collar of the objective lens individually. Images were recorded either as single sections, within z-stacks with 400 nm axial step size, or within time-lapse series, in all of which STED and confocal images were typically acquired quasi-simultaneously (line-by-line) to minimize the influence of drift between the images. In some cases, the confocal EYFP/EGFP morphology reference was acquired separately. SiR-Halo was excited at 640 nm, whereas the far-red FPs were excited by the 594-nm laser. The 775-nm STED laser deexcited both SiR-Halo and the far-red FPs. Fluorescence signals were detected in the dark-red detection channel (685±35 nm) for SiR and in both the red and dark-red detection channels (623±12 nm and 685±35 nm) for the far-red FPs. EGFP and EYFP were excited at 473 nm and imaged in confocal mode in the green-yellow detection channel (525±25 nm).

Image Processing. Displayed images were visualized and processed using the software ImSpector (10). Smoothing was performed using a 2D low-pass Gaussian filter with a width of 1 pixel. Different linear lookup tables ('Magenta', 'Green', and a customized version of 'Magenta') were used for the visualization of image data as indicated. The lower and upper bounds of the lookup tables were adjusted across entire images to make good use of the color scales' central ranges for visual representation, and are indicated in most of the data shown. Note that the count values in the brightest image regions typically exceeded the upper bound *C,* by up to 30 %.

Image Analysis. All quantitative analysis was performed on the basis of raw image data. To determine the width of PSD95 features, an intensity profile (typically an average over 5 pixels perpendicular to the direction of the profile) was measured along the direction of interest in ImSpector. The width of the averaged intensity profile was determined as the FWHM of the Gaussian or Lorentzian curve fitting functions in OriginPro (OriginLab Corp., Northampton, MA, USA). For determinations of spine-head areas (confocal Lifeact-EYFP-labeled spines) and the corresponding superresolved PSD95 scaffold areas, the diameters along the longest and shortest (major and minor) dimensions l and s were estimated by extracting the FWHM from intensity line profiles (averaged over five pixels) in ImSpector. The reported diameters correspond to widths at the height of half the maximum of the outermost intensity peaks of the profile. The estimated areas A were then computed as $A = \pi \cdot s/2 \cdot l/2$.

Semiautomated Analysis of PSD95 Scaffolds. To estimate the dimensions, areas, and filling fractions of a large number of PSD95 scaffold nano-architectures, a custom-written MATLAB routine was used with a two-step analysis process. First, single PSD95 scaffolds were identified within STED images of large fields of view (~15−20 × 15−20 µm²) containing a large variety of PSD95 morphologies. In a second step, this routine estimated morphological characteristics for each identified PSD95 scaffold.

For the identification of PSD95 scaffolds in the recorded images (analysis step 1), low varying background signal originating from out-of-focus structures was removed. To this end, the original image was convolved (smoothed) with a 2D Gaussian peak function of 600 nm FWHM, and 80 % of the intensity in the smoothed image was subtracted from the original image, setting negative values to zero. To reduce noise in the resulting background-corrected image, it was

convolved with a 2D Gaussian peak function of 100 nm FWHM (slightly larger than spatial resolution in in vivo recordings). Then, two thresholds were chosen manually in an iterative procedure for each processed data set. All connected areas in the noise-reduced, background-corrected image consisting of pixel values larger than the first threshold and larger than the second threshold in at least one pixel were regarded as containing a single PSD95 scaffold. This thresholding allowed excluding dark (probably defocused) structures while including the whole area of each desired PSD95 scaffold within a large field of view (*SI Appendix*, Fig. S8*A*). Finally, 5−10 % of the automatically identified PSD95 scaffolds were manually modified (divided, combined or excluded) after visual inspection.

The estimation of morphological characteristics for each PSD95 scaffold (analysis step 2) was performed on the raw image data as follows: Initially, the mean background around a single PSD95 scaffold was estimated from the surrounding area excluding adjacent scaffolds. Then, the original image was de-noised with a 2D Gaussian peak function of 100 nm FWHM and binarized with a threshold being the weighted average of 30 % of the average background value and 70 % of the average value of the de-noised image within the PSD95 scaffold. This threshold produced a cut-off approximately at the center of the slope at the edge of the scaffold. The binary representation defined the locations of protein (protein area) in the identified scaffold while its convex hull was regarded as the scaffold area (*SI Appendix*, Fig. S8*B*, *Middle*). The ratio of the total area of the binary representation and the scaffold area gave the filling fraction (fraction of scaffold area filled by protein). A fit of a homogenously filled 2D ellipse to the binarized PSD95 protein area, maximizing the overlap while minimizing the differences in the areas, and multiple restarts of the optimization with different initial parameters to achieve global convergence, provided short- and long-axis values (*SI Appendix*, Fig. S8*B*, *Right*). The computation of the filling factor, especially the computation of the convex hull, suffered from pixelation effects and was therefore performed on four times linearly interpolated data instead.

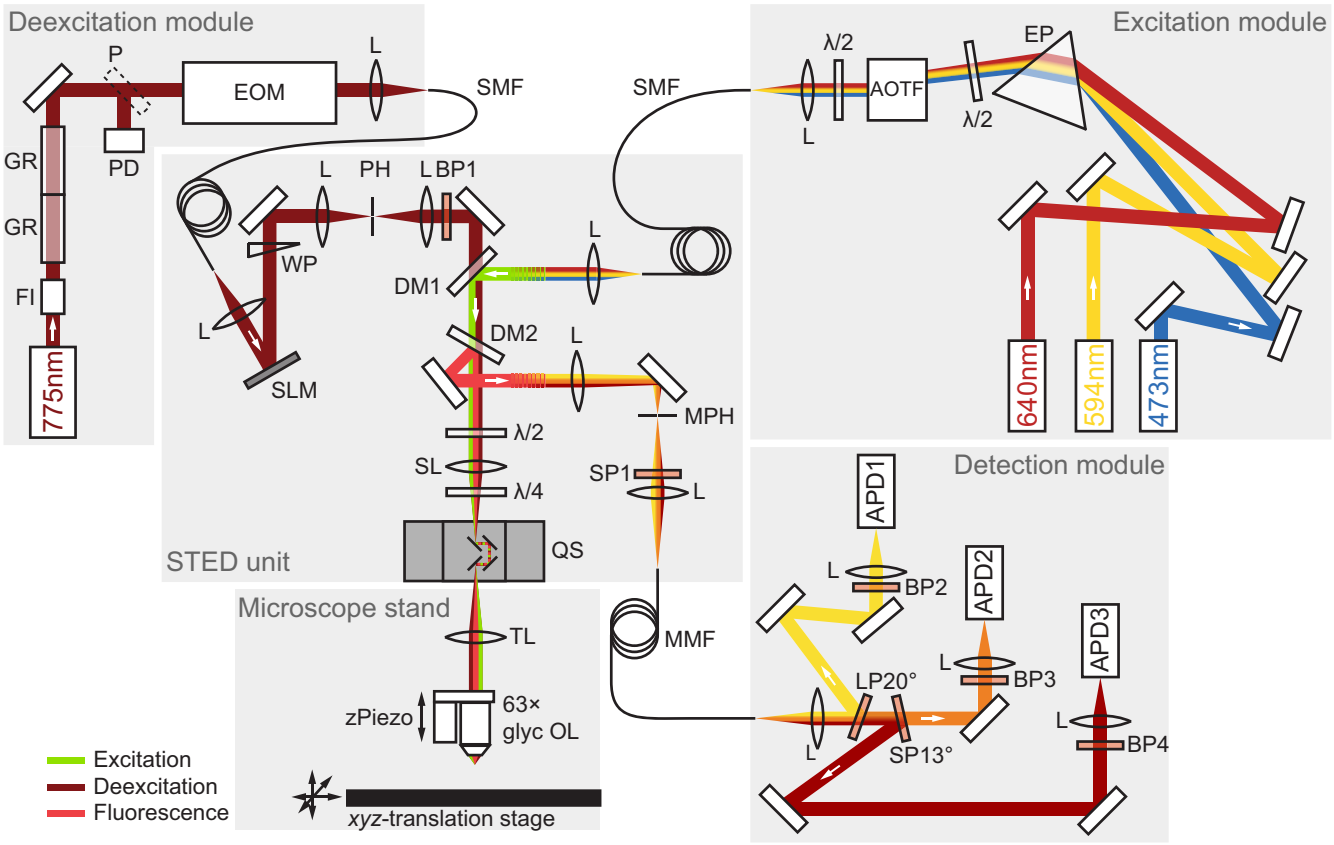

Fig. S1. Scheme of the home-built far-red STED nanoscope for in vivo mouse imaging. λ/2: half-wave plate, λ/4: quarter-wave plate, AOTF: acousto-optic tunable filter, APD: avalanche photo diode, BP: bandpass filter, DM: dichroic mirror, EOM: electro-optic modulator, EP: dispersive equilateral prism, FI: Faraday isolator, GR: glass rod, L: lens, LP: longpass filter, MMF: multi-mode optical fiber, MPH: motorized pinhole, glyc OL: glycerol-immersion objective lens, P: pellicle beam splitter, PD: photodiode, PH: pinhole, QS: Quadscanner, SL: scanning lens, SLM: spatial light modulator, SMF: polarization-maintaining single-mode optical fiber, SP: shortpass filter, TL: tube lens, WP: wedge prism, zPiezo: piezoelectric transducer.

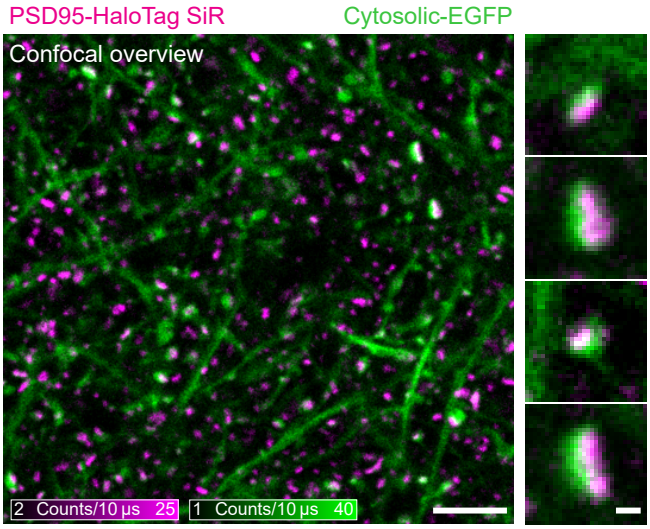

Fig. S2. PSD95 fusion proteins labeled with SiR-Halo in the context of the dendritic morphology visualized by cytosolic volume-filling EGFP. Similar to the Lifeact-EYFP-reference labeling (Fig. 1*D*), pyramidal neurons were transduced with viral particles expressing EGFP as a non-fusion construct. (*Left*) Representative confocal overview image of SiR-Halo-labeled PSD95 (magenta), together with the cytosolic-expressed EGFP (green) in dendrites of the molecular layer in an anaesthetized live mouse about 1 h after ligand injection. White in the overlay corresponds to colocalization of SiR-Halo-labeled PSD95 within spine heads of the morphological reference. (*Right*) Examples of PSD95 with viral-transduction-positive cytosolic EGFP spine heads are shown as magnified views, highlighting different sizes and shapes of PSD95 structural arrangements at limited confocal resolution. The images were smoothed for display with a one-pixel-wide Gaussian filter. Imaging parameters are listed in *SI Appendix*, Table S1. [Scale bars: 5 µm (overview), 500 nm (magnified views)].

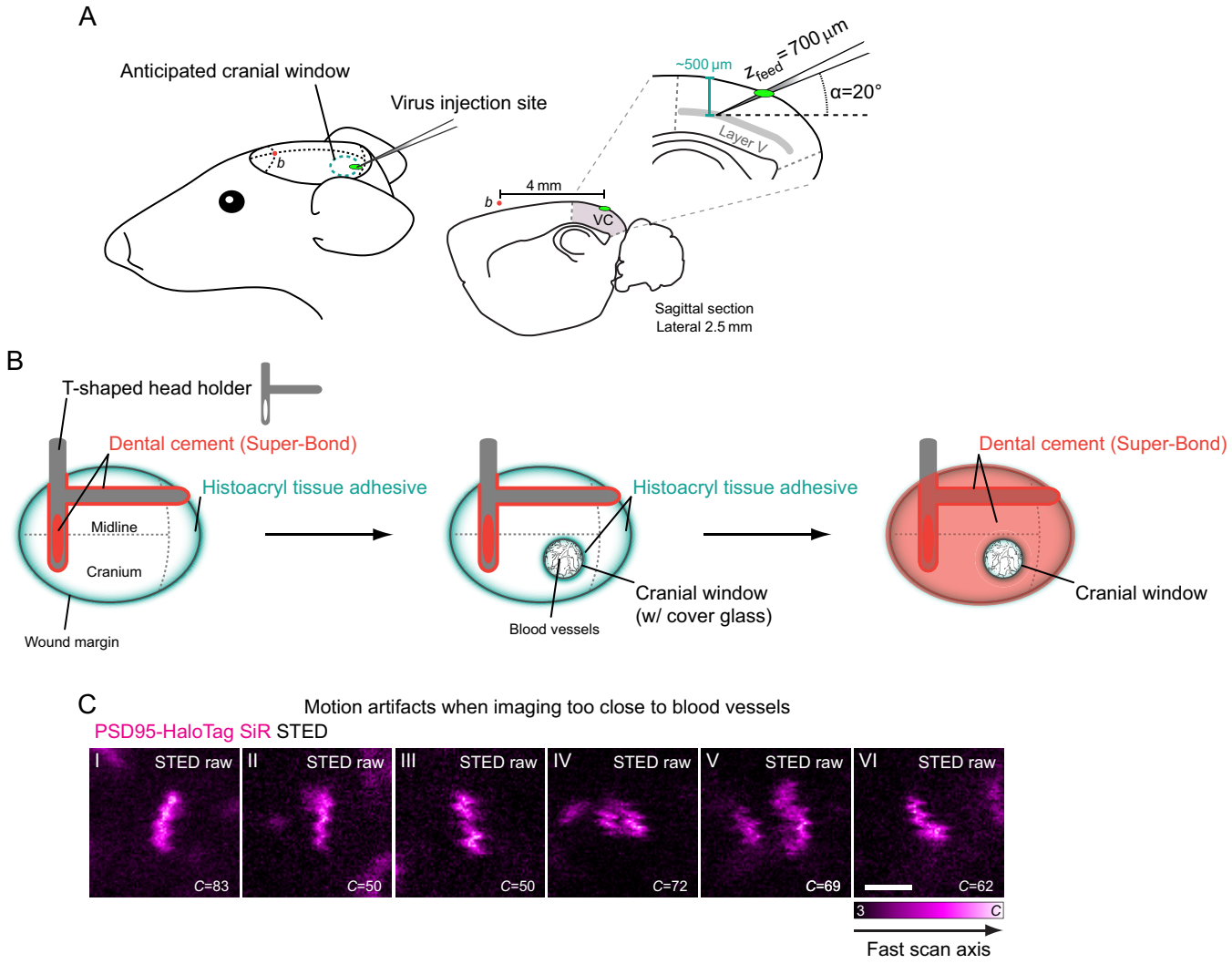

Fig. S3. Schematic views of surgical procedures for in vivo STED imaging. (*A*) Illustration of virus injection into layer V of the visual cortex (VC) for FP expression. Stereotactic injection of recombinant adeno-associated virus was performed at the caudal edge of the designated cranial window location on the left cranial hemisphere, about 4 mm caudal from bregma (*b*, red spot, ref. 4). The glass pipette was inserted at an angle of α=20° to the horizontal plane and with a feed of z_{feed}=700 µm to reach the region containing cell bodies of layer V pyramidal neurons located ~500 µm below the cortical surface of the intended center of the cranial window (magnified view). (*B*) Illustration of the head immobilization and cranial-window fixation. (*Left*) After removing the scalp to get access to the cranium, the wound edges were covered with a thin layer of Histoacryl tissue adhesive (mint, dashed lines indicate cranial sutures) to keep the skull dry. A flat T-shaped head holder (with an oval opening in one arm) was attached using Super-Bond dental cement. (*Middle*) A circular cover glass placed over the cranial hole and the adjacent skull was glued with Histoacryl tissue adhesive to form a cranial window. (*Right*) The complete exposed cranium, wound margins, the edges of the cranial-window cover glass, and the head holder were covered with dental cement for maximal mechanical stabilization. (*C*) Throughout the project, ROIs distant from pulsing blood vessels were selected for imaging, seeking to minimize perturbations from mechanical displacements by pressure modulations in the vascular system. When imaging closer to a blood vessel, the image scan was compromised by highly periodic line-to-line displacements. These displacements were readily appreciated when inspecting imaged structures across the full width of the FOV, with the small magnified views only serving for illustration. A scanned line was acquired in ~15−17 ms. The fast scan axis is indicated. Imaging settings: 5 µW 640-nm excitation power, 66 mW STED power, 15 µm × 15 µm (*I*–*III*) or 10 µm × 10 µm (*IV*–*VI*) FOV, 20-nm pixel size, 30-µs pixel dwell time, resulting in total acquisition times of ~17 s for a large STED frame (*I*–*III*) or 16 s for the examples in (*IV*–*VI*), where a large STED FOV was acquired in line-by-line mode together with the corresponding confocal FOV. Counts stated are counts/30 µs. (Scale bar: 500 nm.)

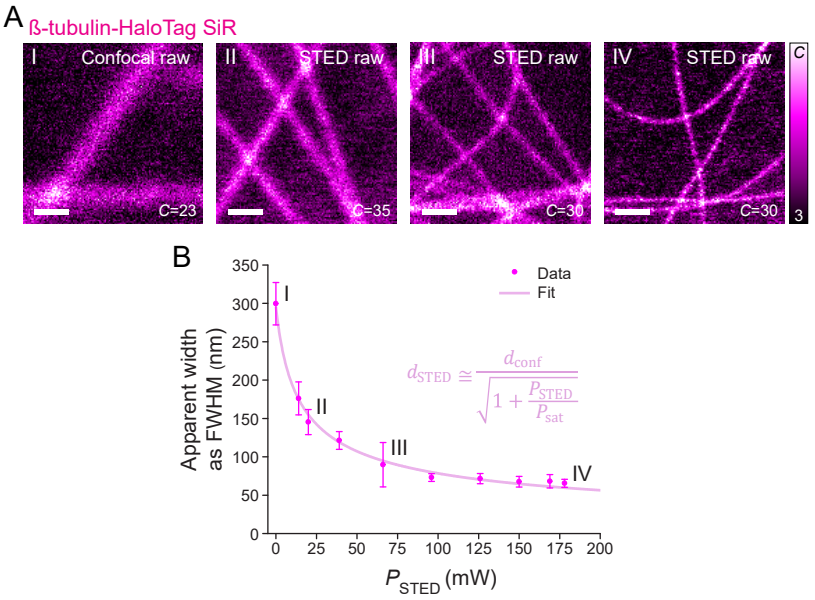

Fig. S4. Resolution scaling with SiR-Halo, illustrated by extracting cross-sectional width of cellular microtubules for different powers of the STED laser. (*A*) β-tubulin of microtubules was labeled with SiR-Halo (1 µM for 20 min) in cultured living Vero cells expressing β-tubulin-HaloTag fusion proteins (plasmid kindly provided by Y. Okada, RIKEN Quantitative Biology Center, Japan) and live-imaged after 20-min washing in confocal mode (*I*), and with STED nanoscopy at increasing STED laser power P_{STED} (*II*–*IV*). (*B*) Apparent width of single tubulin filaments (N=10 for each P_{STED}), FWHM extracted by Gaussian fitting, as a function of P_{STED} approximated by the STED resolution formula with d_{conf}=295.3 nm and P_{sat}=7.6 mW. For P_{STED}=177 mW, the apparent width was 66 ± 5 nm. The diameter of a microtubule on its own is 25 nm, with the HaloTags adding up to 10 nm to the actual diameter (HaloTag size: 3–5 nm based on X ray crystal structure, ref. 11). STED powers were measured at the entrance pupil of the objective lens. Error bars represent SDs. Imaging parameters are listed in *SI Appendix*, Table S1. (Scale bars: 500 nm.)

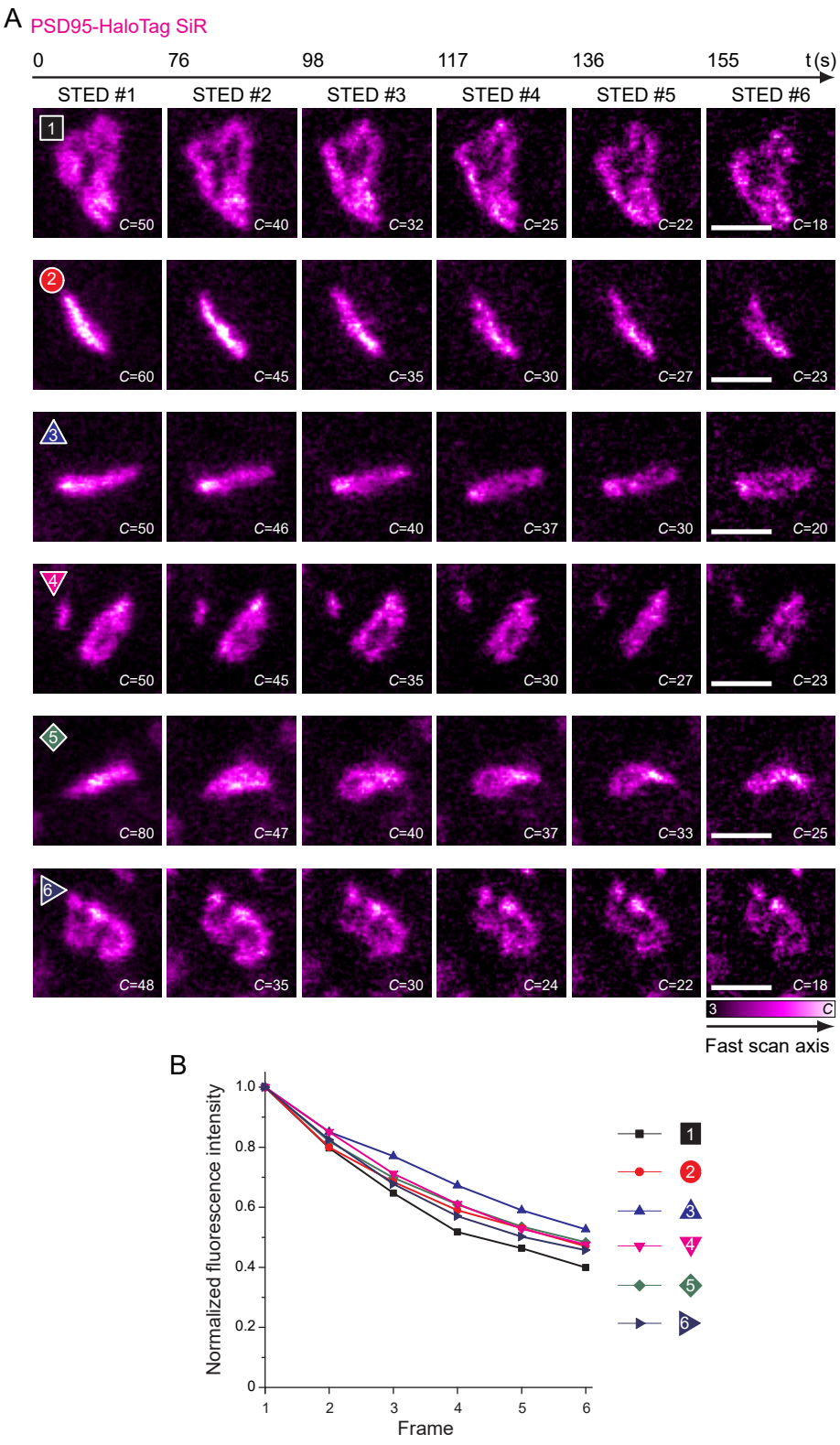

Fig. S5. Photostability of SiR-Halo in in vivo experiments at typical imaging parameters. (*A*) Repeated STED imaging of PSD95 scaffold morphologies. Six frames of 6 examples are displayed. Images represent magnified views from a larger FOV. From the second frame onwards, the large images were acquired during <20 seconds each (portions containing shown image regions: 1.5 s), in direct succession. The large FOV was chosen to simultaneously assess a large number of PSD95 scaffolds. Fast scan axis for all images shown is indicated by an arrow in the bottom right. The images were smoothed for display with a one-pixel-wide Gaussian filter. Imaging parameters are listed in *SI Appendix*, Table S1. (Scale bars: 500 nm.) (*B*) Relative fluorescence intensity in image regions from consecutive STED frames (data in (*A*)). The fluorescence intensity was calculated as the sum of all pixel counts per image region.

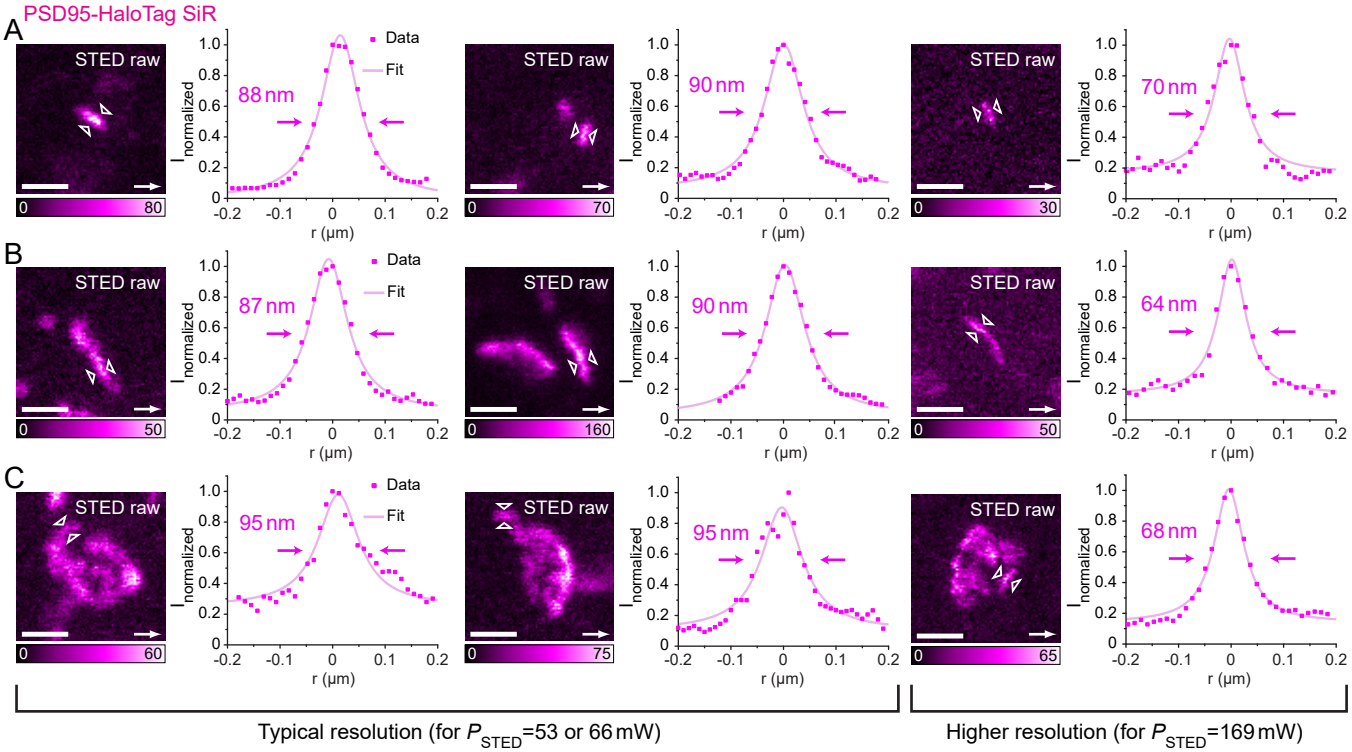

Fig. S6. Examples of smallest apparent widths of PSD95 scaffold features, imaged at the typical ≲90-nm resolution in this study and at higher resolution (≲70 nm). Images represent magnified views extracted from full FOVs of recordings. White arrows indicate the fast scan axis. The widths of small features of (*A*) small round/ovoid, (*B*) thin elongated, and (*C*) complex PSD95 morphologies were measured as FWHMs along the indicated positions, determined by fitting Lorentzian peak functions to the line intensity profiles ($I_{normalized}$, normalized signal intensity; r, distance). Imaging settings: 5−16 µW 640-nm excitation power, 53 or 66 or 169 mW STED power, 5−20 µm × 5−20 µm FOV, 20-nm pixel size, 30-µs pixel dwell time, resulting in total acquisition times of ~6−25 s per large STED frame (or 53 s for the left example in B, where a large FOV was acquired in line-by-line mode). Counts stated are counts/30 µs. (Scale bars: 500 nm.)

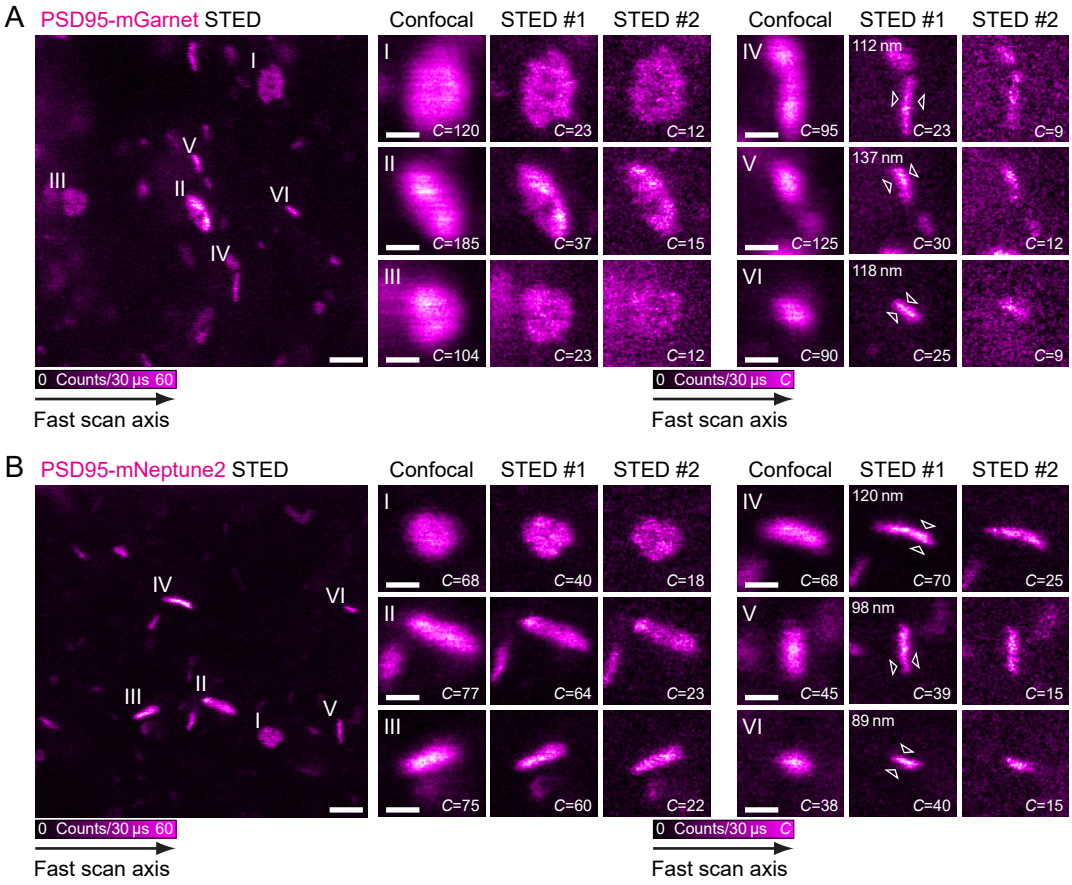

Fig. S7. STED imaging of PSD95 labeled with far-red fluorescent proteins. (*A*) PSD95-mGarnet. (*B*) PSD95-mNeptune2. The respective FPs were fused to the C terminus of PSD95 and expressed by viral-particle transduction. Two consecutive STED recordings are shown next to the confocal recording (all magnified views). A selection of smallest widths (FWHM, extracted by fitting in raw-data images) is indicated. Note that photobleaching significantly reduced the image contrast already in the second STED frame. While the pixel dwell times were 30 µs as for SiR-Halo recordings, the powers differed: excitation powers were about twofold (mNeptune2) or on average ~sixfold (mGarnet) higher and STED powers were about half compared to those used in the SiR-Halo experiments. Complex-shaped PSD95 scaffolds (*A*,*I–III* and *B*,*I*) did not exhibit clearly resolved internal structure. The arrows indicate the fast scan axis. The images were smoothed for display with a one-pixel-wide Gaussian filter. The corresponding EYFP morphological reference images are not displayed. Imaging parameters are listed in *SI Appendix*, Table S1. [Scale bars: 1 µm (overviews), 500 nm (magnified views).]

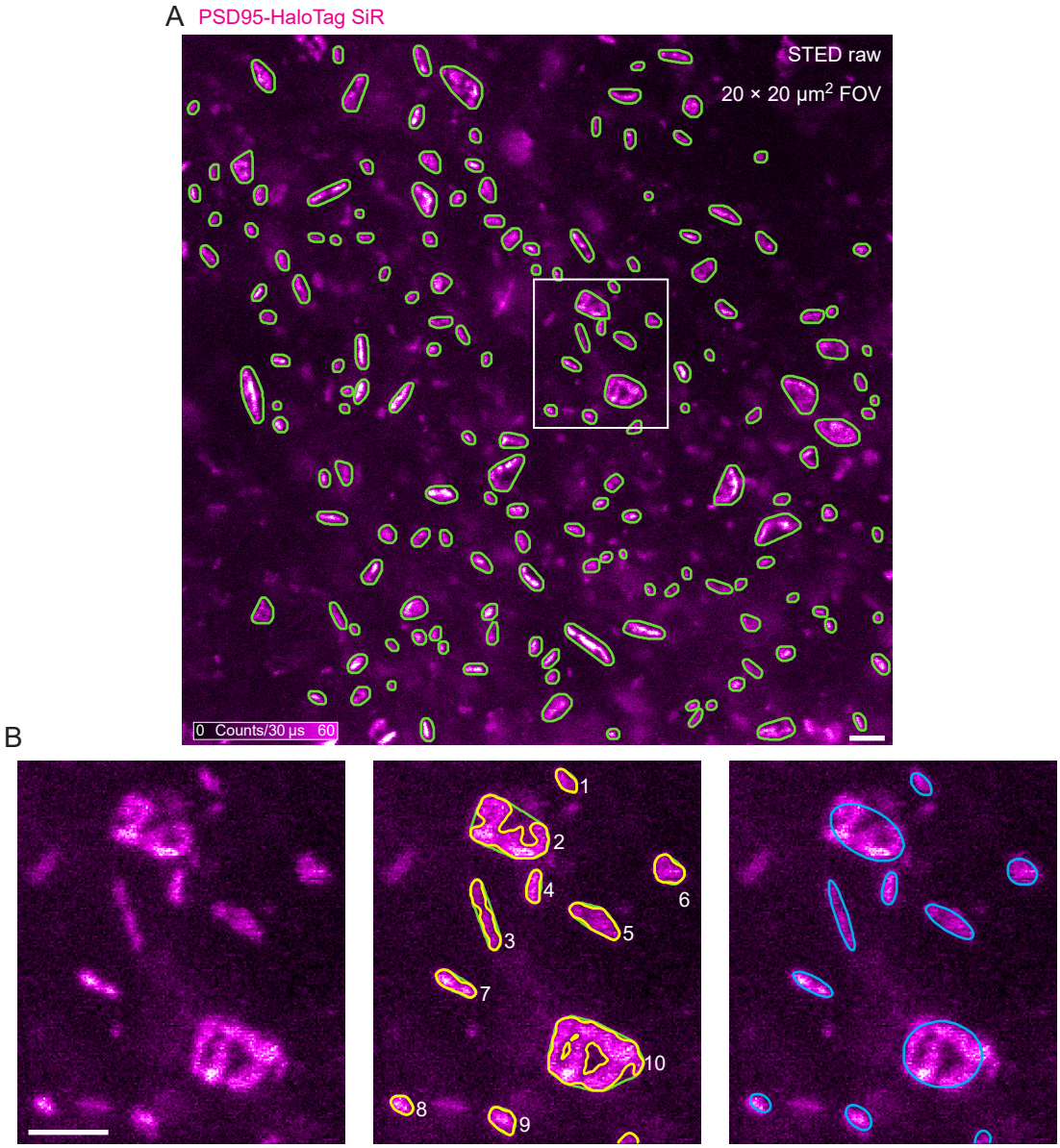

C

PSD95 scaffold	Scaffold area (µm²)	Protein area (µm²)	Filling fraction	Short axis (nm)	Long axis (nm)	Small round/ovoid or large
1	0.047	0.046	0.97	181	317	Small round/ovoid
2	0.429	0.315	0.73	523	900	Large
3	0.133	0.113	0.84	152	856	Large
4	0.057	0.054	0.95	176	389	Small round/ovoid
5	0.132	0.123	0.93	225	630	Large
6	0.090	0.086	0.96	292	356	Small round/ovoid
7	0.080	0.075	0.93	180	509	Large
8	0.046	0.045	0.98	186	274	Small round/ovoid
9	0.073	0.069	0.95	228	349	Small round/ovoid
10	0.621	0.501	0.81	739	884	Large

Fig. S8. Demonstration of the semiautomated analysis of the PSD95 scaffolds. (*A*) Identification of the individual PSD95 scaffolds (outlined, green). (*B*) *Left*: Magnified view of the region marked in (A). *Middle*: Additionally, outlines of the estimated protein area (yellow) as well as the entire scaffold area (green). *Right*: Fitted elliptic shapes (outlined, blue) for short- and long-axis diameter estimations. (*C*) Examples of analysis results of morphological characteristics for the identified PSD95 scaffolds presented in the magnified views in (*B*). (Scale bars: 1 µm.)

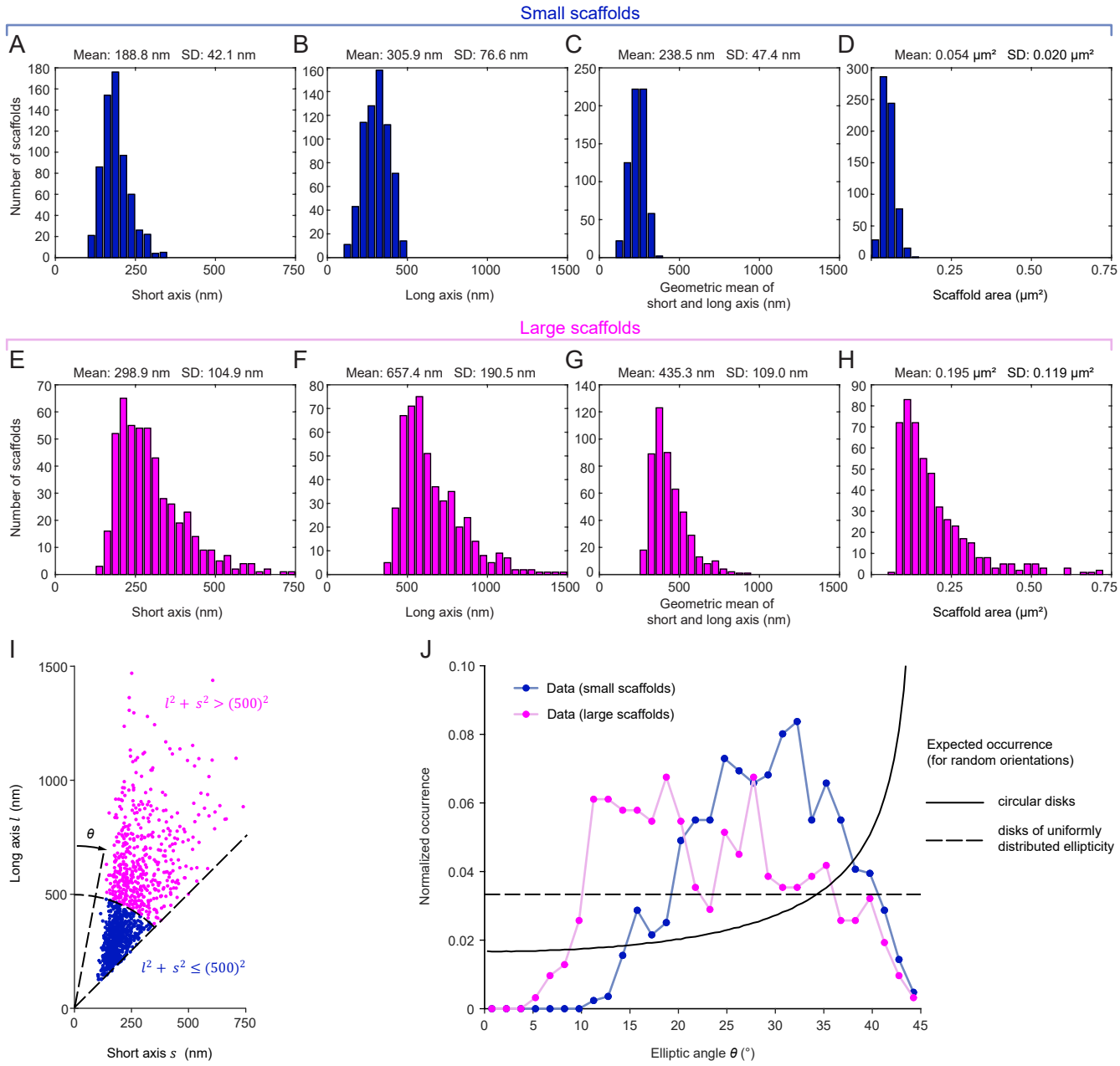

Fig. S9. Histograms of scaffold dimensions and areas, and geometrical argument regarding observed scaffold ellipticities. Frequency plots of (*A, E*) short-axis diameters, (*B, F*) long-axis diameters, (*C, G*) average diameters computed as the geometric means of the respective short and long axes, and (*D, H*) scaffold areas for small (*A–D*) and large (*E–H*) scaffolds [definitions see (*I*)]. (*I*) Data from Fig. 4*A* displayed as scatter plot, with definitions of small and large scaffold categories and definition of the elliptic angle θ in the analysis of (*J*). (*J*) Normalized histograms of scaffold numbers falling within bins of elliptic angle $\theta = 90° - \arctan$ (ellipticity), with ellipticity being the ratio of long-axis diameter l and short-axis diameter s, for all PSD95 scaffold nano-architecture images for the two categories with the definitions in (*I*). An elliptic angle of $\theta = 45°$ corresponds to perfectly round-appearing scaffolds and an elliptic angle close to $\theta = 0°$ to thin, elongated appearances. Every angle represents a fixed ratio of long-axis and short-axis diameter. The finite optical resolution explains the absence of scaffolds observed with very small elliptic angles. Perfectly round, flat structures can also appear elliptical (due to the relative orientation of the imaging plane), with the 2D projection effect leading to an expected occurrence histogram (solid black line), with most expected observations at $\theta = 45°$. If all values of ellipticity were equally probable for the scaffolds, and accounting for all possible orientations, a flat histogram across elliptic angles would be expected (dashed black line), but such a distribution of ellipticities was not observed.

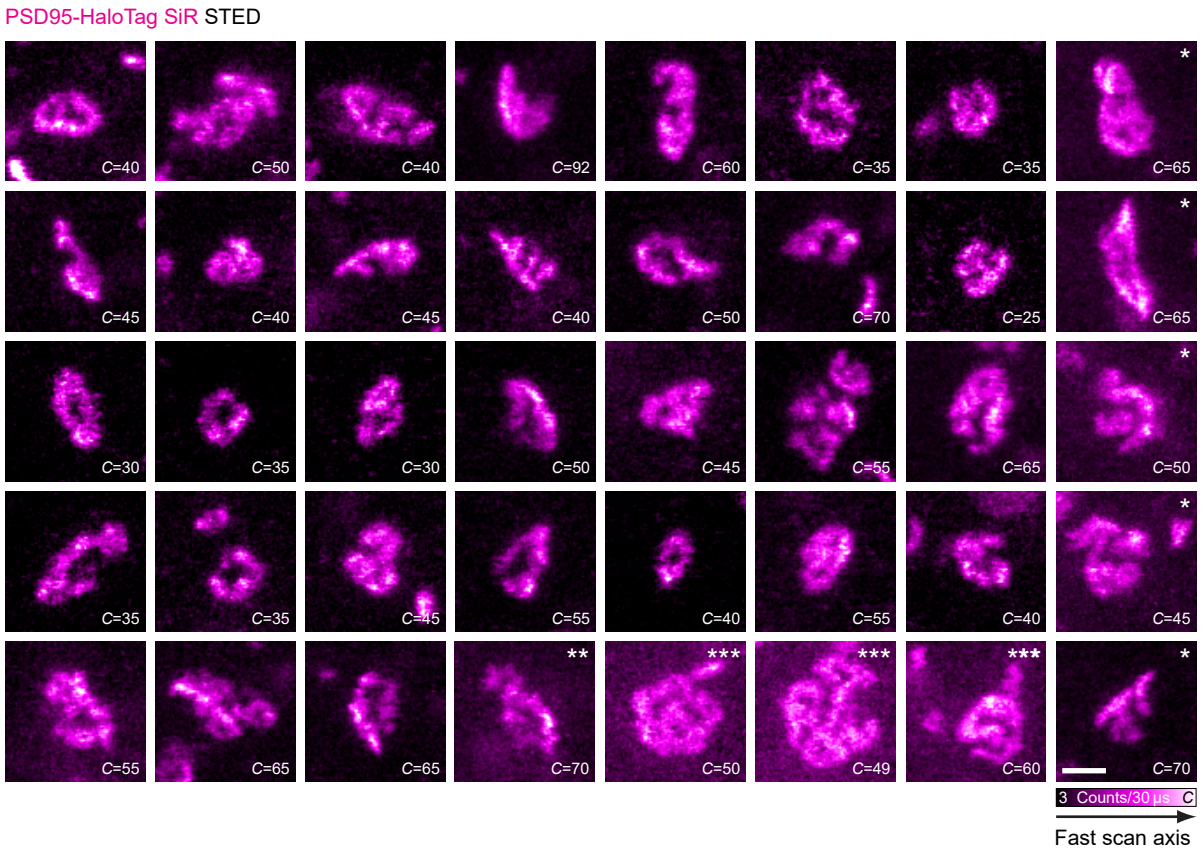

Fig. S10. More examples of complex-shaped PSD95 architectures. Images represent magnified views extracted from full FOVs of recordings. Imaging settings: 3−16 µW 640-nm excitation power, 53 or 66 mW STED power (*: 82 mW, **: 96 mW, ***: 126 mW), 5−18 × 5−18 µm² FOV, 20-nm pixel size, 30-µs pixel dwell time, resulting in total acquisition times of ~6−26 s per large STED frame for sequential acquisition of STED and confocal channels (27 image regions shown). In other experiments, ~6−53 s were spent acquiring the confocal morphology reference, the confocal PSD95 image as well as the STED PSD95 image together in line-by-line acquisition mode (13 image regions shown). The arrow at the bottom right indicates the fast scan axis for all images shown. The images were smoothed for display with a one-pixel-wide Gaussian filter. (Scale bars: 500 nm.)

Table S1. Image Acquisition Parameters

Figure	Pixel size in x, y (nm) (x: fast scan axis, y: slow scan axis)	Full field of view of recording (µm×µm for fast×slow scan axes)	Pixel dwell time (µs)	Total acquisition time of image series (s)	Acquisition time of single STED image portion containing a magnified view (s; µm×µm for fast×slow scan axes)	Acquisition mode and sequence	Excitation power† and wavelength (µW) / (nm)	STED power† (mW)
Fig. 1D						Line-by-line:		
	200	127×127	10	9.1	-	Conf_SiR,	<1 / 640	-
	200	127×127	10		-	Conf_eYFP	<1 / 473	-
Fig. 2A						Sequential:		
	20	20×20	20	20.8	-	Conf_eYFP	<1 / 473	-
	20	20×20	10	10.8	-	Conf_SiR	9 / 640	-
	20	20×20	30	30.8	2.0; 20×1.6	STED_SiR	9 / 640	66
Fig. 3A, I						Sequential:		
	20	17×17	20	14.8	-	Conf_SiR	9 / 640	-
	20	17×17	20	14.8	-	Conf_eYFP	<1 / 473	-
	20	17×17	30	21.9	2.1; 17×1.6	STED_SiR	9 / 640	53
Fig. 3A, II						Line-by-line:		
	20	15×15	30	52.8	5.6; 15×1.6	STED_SiR	5 / 640	66
	20	15×15	30		-	Conf_SiR	5 / 640	-
	20	15×15	30		-	Conf_eYFP	<1 / 473	-
Fig. 3A, III						Sequential:		
	20	10×10	10	3.0	-	Conf_SiR	9 / 640	-
	20	10×10	30	8.1	1.3; 10×1.6	STED_SiR	9 / 640	66
	20	10×10	20	5.5	-	Conf_YFP	<1 / 473	-
Fig. 3A, IV						z-stack with 5 sections		
						Line-by-line:		
	20	10×10	30	120.5	3.8; 10×1.6	STED_SiR	5 / 640	66
	20	10×10	30		-	Conf_SiR	5 / 640	-
	20	10×10	30		-	Conf_eYFP	<1 / 473	-
Fig. 3B, I						Line-by-line:		
	20	15×15	30	52.8	5.6; 15×1.6	STED_SiR	5 / 640	66
	20	15×15	30		-	Conf_SiR	5 / 640	-
	20	15×15	30		-	Conf_eYFP	<1 / 473	-
Fig. 3B, II						Line-by-line:		
	20	15×15	30	52.8	5.6; 15×1.6	STED_SiR	5 / 640	66
	20	15×15	30		-	Conf_SiR	5 / 640	-
	20	15×15	30		-	Conf_eYFP	<1 / 473	-
Fig. 3B, III						Line-by-line:		
	20	15×15	30	52.8	5.6; 15×1.6	STED_SiR	5 / 640	66
	20	15×15	30		-	Conf_SiR	5 / 640	-
	20	15×15	30		-	Conf_eYFP	<1 / 473	-
Fig. 3B, IV						z-stack with 5 sections		
						Line-by-line:		
	20	10×10	30	120.5	3.8; 10×1.6	STED_SiR	5 / 640	66
	20	10×10	30		-	Conf_SiR	5 / 640	-
	20	10×10	30		-	Conf_eYFP	<1 / 473	-
Fig. 3C, I						z-stack with 5 sections		
						Line-by-line:		
	20	10×10	30	120.5	3.8; 10×1.6	STED_SiR	5 / 640	66
	20	10×10	30		-	Conf_SiR	5 / 640	-
	20	10×10	30		-	Conf_eYFP	<1 / 473	-
Fig. 3C, II						Sequential:		
	20	15×15	10	17.0	-	Conf_SiR	5 / 640	-
	20	15×15	30	17.0	1.9; 15×1.6	STED_SiR	5 / 640	66
	20	15×15	30	17.0	-	Conf_eYFP	<1 / 473	-
Fig. 3C, III						Sequential:		
	20	17×17	20	14.8	-	Conf_SiR	9 / 640	-
	20	17×17	20	14.8	-	Conf_eYFP	<1 / 473	-
	20	17×17	30	21.9	2.1; 17×1.6	STED_SiR	9 / 640	53

Fig. 3C, IV						Line-by-line:			
	20	15×10	30		5.6; 15×1.6	STED_SiR	3 / 640	126
	20	15×10	30	33.3	-	Conf_SiR	3 / 640	-
	20	15×10	30		-	Conf_eYFP	<1 /473	-
Fig. 3C, V						Sequential:		
	20	10×10	10	3.0	-	Conf_SiR	9 / 640	-
	20	10×10	30	8.1	1.3; 10×1.6	STED_SiR	9 / 640	66
	20	10×10	20	5.5	-	Conf_YFP	<1 / 473	-
Fig. 3C, VI						Line-by-line:		
	20	15×10	30		5.6; 15×1.6	STED_SiR	3 / 640	126
	20	15×10	30	33.3	-	Conf_SiR	3 / 640	-
	20	15×10	30		-	Conf_eYFP	<1 / 473	-
Fig. 5A						*z*-stack with 3 sections Line-by-line:		
	20	15×15	30		5.6; 15×2.5	STED_SiR	5 / 640	82
	20	15×15	30	158.2	-	Conf_SiR	5 / 640	-
	20	15×15	30		-	Conf_eYFP	<1 / 473	-
Fig. S2						Line-by-line:		
	80	54×54	10	10.1	-	Conf_SiR	<1 / 640	-
	80	54×54	10		-	Conf_eYFP	<1 / 473	-
Fig. S4A, I	20	19×17	20	8.6	-	Conf_SiR	5 / 640	-
Fig. S4A, II	20	18×13	20	6.4	1.3; 18×2.6	STED_SiR	5 / 640	20
Fig. S4A, III	20	12×14	20	4.8	0.9; 12×2.6	STED_SiR	5 / 640	66
Fig. S4A, IV	20	17×19	20	9.0	1.2; 17×2.6	STED_SiR	17 / 640	177
Fig. S5A, #1						Line-by-line:		
	20	15×15	30		4.6; 15×1.3	STED_SiR	5 / 640	66
	20	15×15	30	52.8	-	Conf_SiR	5 / 640	-
	20	15×15	30		-	Conf_eYFP	<1 / 473	-
Fig. S5A, #2–#6	20	15×15	30	17.6	1.5; 15×1.6	STED_SiR	5 / 640	66
Fig. S7A, #1						Line-by-line:		
	20	10×10	30		3.8; 10×1.6	STED_mGarnet	40 / 594	39
	20	10×10	30	23.7	-	Conf_ mGarnet	40 / 594	-
	20	10×10	30		-	Conf_eYFP	30 / 473	-
Fig. S7A, #2	20	10×10	30	7.9	1.3; 10×1.6	STED_mGarnet	40 / 594	39
Fig. S7B, #1						Sequential:		
	20	12×10	30	9.0	1.5; 12×1.6	STED_ mNeptune2	13 / 594	30
	20	12×10	30	9.0	-	Conf_ mNeptune2	13 / 594	-
	20	12×10	10	3.3	-	Conf_eYFP	<1 / 473	-
Fig. S7B, #2	20	12×10	30	9.0	1.5; 12×1.6	STED_ mNeptune2	13 / 594	30

[†]All stated laser powers were measured at the entrance pupil of the objective lens.

References

1. Hirrlinger PG, et al. (2005) Expression of reef coral fluorescent proteins in the central nervous system of transgenic mice. *Mol Cell Neurosci* 30:291–303.
2. Willig KI, et al. (2014) Nanoscopy of Filamentous Actin in Cortical Dendrites of a Living Mouse. *Biophys J* 106:L01−L03.
3. Hense A, et al. (2015) Monomeric Garnet, a far-red fluorescent protein for live-cell STED imaging. *Sci Rep* 5:18006.
4. Paxinos G, Franklin K (2007) *The Mouse Brain in Stereotaxic Coordinates* (Elsevier, New York, USA) 3rd Ed.
5. Berning S, Willig KI, Steffens H, Dibaj P, Hell SW (2012) Nanoscopy in a Living Mouse Brain. *Science* 335:551.
6. Lukinavičius G, et al. (2013) A near-infrared fluorophore for live-cell super-resolution microscopy of cellular proteins. *Nat Chem* 5:132−139.
7. Henrich MB (2014) The Potential of Semiconductor Lasers for STED Nanoscopy. Dissertation, University of Heidelberg.
8. Engelhardt J (2010) Method and device for dynamically shifting a light beam relative to an optic which focuses the light beam. Patent application WO2010069987 A1(WO2009EP67269 20091216).
9. Görlitz F, et al. (2014) A STED Microscope Designed for Routine Biomedical Applications. *Prog Electromagn Res* 147:57−68.
10. Schönle A (2006) Imspector Image Acquisition & Analysis Software, v0.10 (http://www.imspector.de).
11. Liu Y, et al. (2017) AgHalo: A Facile Fluorogenic Sensor to Detect Drug-Induced Proteome Stress. *Angew Chem Int Ed Engl* 56:8672−8676.